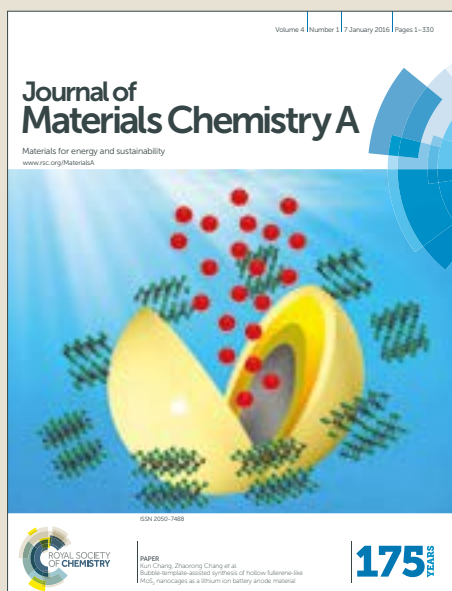


Journal of Materials Chemistry A

Accepted Manuscript



This article can be cited before page numbers have been issued, to do this please use: T. Meng, J. Qin, S. Wang, D. Zhao, B. Mao and M. Cao, *J. Mater. Chem. A*, 2017, DOI: 10.1039/C7TA01453H.



This is an Accepted Manuscript, which has been through the Royal Society of Chemistry peer review process and has been accepted for publication.

Accepted Manuscripts are published online shortly after acceptance, before technical editing, formatting and proof reading. Using this free service, authors can make their results available to the community, in citable form, before we publish the edited article. We will replace this Accepted Manuscript with the edited and formatted Advance Article as soon as it is available.

You can find more information about Accepted Manuscripts in the [author guidelines](#).

Please note that technical editing may introduce minor changes to the text and/or graphics, which may alter content. The journal's standard [Terms & Conditions](#) and the ethical guidelines, outlined in our [author and reviewer resource centre](#), still apply. In no event shall the Royal Society of Chemistry be held responsible for any errors or omissions in this Accepted Manuscript or any consequences arising from the use of any information it contains.

In Situ Coupling of Co_{0.85}Se and N-Doped Carbon via One-Step Selenizing of Metal–Organic Frameworks as Trifunctional Catalysts for Overall Water Splitting and Zn–air Batteries

Tao Meng, Jinwen Qin, Shuguang Wang, Di Zhao, Baoguang Mao, Minhua Cao*

Received 00th January 20xx,
Accepted 00th January 20xx

DOI: 10.1039/x0xx00000x

www.rsc.org/

Developing efficient noble metal-free multifunctional electrocatalysts is highly effective to dramatically reduce the overall cost of the electrochemical devices. In this work, we for the first time demonstrate a facile strategy for *in situ* coupling of ultrafine Co_{0.85}Se nanocrystals and N-doped carbon (Co_{0.85}Se@NC) by directly selenizing zeolitic imidazolate framework-67 (ZIF-67) polyhedrons. Benefiting from the synergistic effect of the coupling between Co_{0.85}Se and NC, the Co–N–C structure, and the porous conductive carbon network, Co_{0.85}Se@NC affords excellent oxygen evolution reaction (OER) performance with small overpotential, remarkable stability, and high Faradaic efficiency. Furthermore, Co_{0.85}Se@NC can also efficiently catalyze hydrogen evolution reaction (HER) and oxygen reduction reaction (ORR), and we therefore investigated its applications as trifunctional electrocatalysts for overall water splitting and Zn–air batteries. When used as both the anode and cathode for overall water splitting, a low cell voltage of 1.76 V is required to reach the current density of 10 mA cm⁻²; the obtained Zn–air batteries exhibit a very low discharge–charge voltage gap (0.80 V at 10 mA cm⁻²) and long cycle life (up to 180 cycles). These results not only demonstrate a facile strategy for the synthesis of affordable Co_{0.85}Se@NC but also present its huge potential as trifunctional electrocatalysts for clean energy systems.

Introduction

Growing global energy consumption and associated environmental issues have motivated a considerable interest in clean energy systems, such as, water splitting devices, rechargeable metal–air batteries, and fuel cells. The electrocatalytic reactions involved in these energy systems [e.g. hydrogen evolution reaction (HER), oxygen reduction reaction (ORR), especially core oxygen evolution reaction (OER)] all require high-performance electrocatalysts to promote their commercial applications.^{1–3} Nowadays the state-of-the-art electrocatalysts for OER, HER, and ORR are still noble metals, such as Ir, Ru, Pt and so on.^{4–6} However, the prohibitive costs and scarcity of these noble metals seriously hinder their large-scale commercial use. Therefore, much effort has been devoted to searching for noble metal-free electrocatalysts with performances comparable to those in the noble metals. Recently, cobalt selenides, as a type of highly active cobalt (Co)-based electrocatalysts,^{3,7–16} have attracted considerable attentions due to their low cost, environmental friendliness, and high thermal and chemical stability. And a variety of strategies have been developed to improve their performance. For instance, Xie's group designed and prepared vacancy-rich ultrathin CoSe₂ nanosheets with enhanced OER activity.¹² Yu's group reported that CoSe₂/Mn₃O₄ and CoSe₂/CeO₂ hybrids display significantly improved OER performances compared

to pristine CoSe₂.^{11,13} Zhang's group achieved bifunctional overall water splitting by anchoring CoO domains on CoSe₂ nanobelts.¹⁴ Cui's group constructed an efficient and stable HER electrocatalyst by growing CoSe₂ nanoparticles (NPs) on carbon fibre paper.¹⁵ And, Co_{0.85}Se/graphene hybrid was also used as a highly efficient catalyst for ORR.¹⁶ In spite of these remarkable electrocatalytic behaviors in OER or HER or ORR mentioned above, few cobalt selenide electrocatalysts can function well toward all OER, HER and ORR in a same electrolyte because of their unstable or inactive property in unfavorable pH environment.^{14,17} Therefore, constructing cobalt selenides with integrated performance for clean energy systems, such as, overall water splitting and rechargeable zinc–air batteries is still a challenging work.

Recently, a new family of metal–organic frameworks (MOFs)-derived materials, including porous carbon and metal-based/(heteroatom-doped) carbon hybrid nanocomposites have drawn fast-growing interests, and they have been widely used in electro-catalysis, electrochemical energy storage, and other fields.^{2,3,18–21} The MOFs as both the precursor and template can afford abundant channels to facilitate electron/ion transport or provide (heteroatom-doped) carbon species to combine with metal species by *in situ* carbonization to further increase the relevant properties (i.e. active sites, conductivity, and adsorptivity).^{22–24} Besides, the huge families of MOFs, which can be obtained easily by changing metal species and organic ligands, also enrich these precursors and templates. On the other hand, the novel and high-performance electrocatalysts like MoC_x,² especially those Co-based groups, such as Co₃O₄-carbon hybrid,³ Co-C@Co₉S₈ double-shelled nanocages,²⁵ and Co_xFe_{1-x}P,²⁶ have been successfully obtained by

Key Laboratory of Cluster Science, Ministry of Education of China, Beijing Key Laboratory of Photoelectronic/Electrophotonic Conversion Materials, School of Chemistry and Chemical Engineering, Beijing Institute of Technology, Beijing 100081, P. R. China. *E-mail: caomh@bit.edu.cn

using corresponding MOFs. Nowadays, zeolitic imidazolate framework-67 (ZIF-67), a type of common MOFs, has been used as the precursor to prepare some functional materials, especially the electrocatalysts like Co@Co₃O₄/NC,²⁷ Co-C@Co₉S₈,²⁵ CoP,^{28,29} and ZIF-Co_{0.85}Se.³⁰ However, these materials suffer from a time-consuming, multi-step synthetic process, or cannot work well as trifunctional electrocatalysts in OER, HER, and ORR. Also, cobalt selenide derived from MOFs as an electrocatalyst has rarely reported so far.

The materials with metal–nitrogen–carbon (Me–N–C) structure, *i.e.* metal cations being coordinated with nitrogen functional groups provided by organic ligands or N-doped carbon, have been demonstrated to be high-performance electrocatalysts because of their excellent electroactivity and strong durability.^{5,31–36} Thus, extensive works have been directed to those electrocatalysts with the Me–N–C structure for OER, HER, and ORR. For instance, Co–N–C species originating from N-doped Co₉S₈/graphene hybrid³¹ and Co encapsulated in nitrogen-doped carbon nanotubes³⁶ can boost both OER and ORR performances; NiO combined with Fe(Co)–N–C⁵ and Ti–N_x–C³² constructed by the interaction between the carbon nitride and the titanium carbide nanosheets can enhance the OER activity. However, these strategies all suffer from a multi-step, time-consuming preparation process, or a high-temperature thermal treatment. Therefore, above cases inspire us to seek for advanced yet simple method to obtain the catalysts with the Me–N–C structure for efficiently enhancing the electro-catalysis performance. Thus, a promising fabrication strategy is produced by using MOFs with N-rich organic ligand followed by one-step carbonization to ensure the resultant electrocatalysts with the Me–N–C (*e.g.* Co–N–C) structure and controlled microstructure.

Herein, we, for the first time, demonstrated *in situ* coupling of Co_{0.85}Se nanocrystals and N-doped carbon (denoted as Co_{0.85}Se@NC) via one-step carbonization–selenylation procedure by using zeolitic imidazolate framework-67 (ZIF-67) as both the precursor and the template. The resultant Co_{0.85}Se@NC can be used as trifunctional electrocatalysts for overall water splitting and Zn–air batteries. Importantly, the carbonization of ZIF-67 not only can provide N-doped carbon combining with Co_{0.85}Se nanocrystals to afford a synergistic effect, but also can construct the Co–N–C structure to further enhance the multifunctional electrocatalysis performances. Besides, the *in situ* carbonization of ZIF-67 can also ensure the smaller size of Co_{0.85}Se nanocrystals to increase the catalytic sites, thus resulting in a high electrocatalytic activity. Additionally, the resultant Co_{0.85}Se@NC also inherits the porous structure of the ZIF-67 template, which can increase the solid/liquid contact surface area and promote the efficient transfer of the electrolyte and the rapid diffusion of gas products. As a consequence, Co_{0.85}Se@NC with the Co–N–C structure, the short diffusion pathways for electron/ion transport, and the synergistic effect between the ultrafine Co_{0.85}Se nanocrystals and NC, exhibits excellent activity as trifunctional electrocatalysts for overall water splitting and rechargeable Zn–air batteries.

Experimental

Preparation of ZIF-67

In a typical synthesis, 0.63 mmol of Co(NO₃)₂·6H₂O was first dissolved into 50 mL of ethanol under magnetic stirring. Then, 50 mL of ethanol containing 2.48 mmol of 2-methylimidazole was dropwise added into the above solution under continuous stirring, and the resultant solution was further stirred at room temperature. After 24 h, the product (ZIF-67) was collected by centrifuging, washed with absolute ethanol, and then dried at 80 °C for 12 h.

Preparation of Co_{0.85}Se@NC

To prepare Co_{0.85}Se@NC, the obtained ZIF-67 and Se powder with a mass ratio of 1:1 were put in two separate positions of a porcelain boat. Then the porcelain boat was put into a furnace with Se powder at the upstream side of the furnace and heated at 600 °C for 3 h with a heating speed of 2 °C min⁻¹ under H₂/Ar atmosphere (H₂, 7 vol%). After being cooled to room temperature, Co_{0.85}Se@NC was obtained. For comparison, another two Co_{0.85}Se@NC samples were also prepared at 500 °C and 700 °C while keeping other reaction conditions constant.

Preparation of Co_{0.85}Se

ZIF-67 was first calcined at 500 °C for 3 h with a heating speed of 2 °C min⁻¹ in air, leading to the formation of Co₃O₄. Then Co₃O₄ and Se were reacted with the reaction parameters same as those for the preparation of Co_{0.85}Se@NC.

Preparation of N-doped carbon (named as NC)

NC was prepared by etching the as-prepared Co_{0.85}Se@NC with 1.0 M HCl aqueous solution for 24 h to remove Co_{0.85}Se.

Preparation of physically mixed Co_{0.85}Se and NC

The as-prepared Co_{0.85}Se was physically mixed with NC in a mass ratio same as that for Co_{0.85}Se@NC by grinding and ultrasound treatment.

Preparation of CoSe₂@NC

CoSe₂@NC was prepared with a mass ratio of ZIF-67 to Se powder at 1:2 while keeping other reaction conditions same as those of Co_{0.85}Se@NC.

Preparation of Co@NC

ZIF-67 was directly heated at 600 °C for 3 h with a heating speed of 2 °C min⁻¹ under H₂/Ar atmosphere (H₂, 7 vol%).

Materials characterizations

Powder X-ray diffraction (XRD) analysis was performed on a Bruker D8 Advance diffractometer with Cu–K α radiation ($\lambda \approx 0.154$ nm) at 40 kV and 40 mA in a scanning range of 10°–80° (2 θ). Raman spectra were collected on an Invia Raman spectrometer with a excitation laser wavelength of 633 nm. The thermogravimetric analysis (TG) was performed on a Rigaku thermogravimetry (TG) analyser from the room temperature to 800 °C with a heating rate of 20 °C min⁻¹ in air. X-ray spectroscopy (XPS) was performed on the ESCALAB 250 spectrometer (Perkin–Elmer). The X-ray absorption near edge structure (XANES) measurements were undertaken at Beamlines 1W1B at Beijing Synchrotron Radiation Facility (BSRF) using transmission modes. The morphologies of as-obtained products were observed on field emission scanning electron microscopy (FE-SEM, HITACHI S-4800). Transmission electron

microscopy (TEM) and high-resolution TEM (HRTEM) were performed on a JEOL JEM-2010 microscopes. Energy dispersive spectroscopy (EDS) element mapping images were taken on scanning transmission electron microscope (STEM) (FEI Technai G2 F20). N₂ adsorption-desorption isotherms were measured on a Belsorp-max sorption analyzer at liquid nitrogen temperature (77 K). Before measurement, the Co_{0.85}Se@NC sample was degassed at 200 °C for 3 h. Surface area was calculated by the multi-point Brunauer–Emmett–Teller (BET) method. The pore-size distribution was calculated from the adsorption branch using the Barrett–Joyner–Halenda (BJH) model.

Electrode preparation and electrochemical characterizations

Preparation of electrocatalyst ink

The working electrodes for electrochemical measurements were prepared by following processes. 4 mg of the as-prepared sample was dispersed into 1 mL of solution containing 900 μL of ethanol and 100 μL of 0.5 wt% Nafion solution and followed by ultrasonic treatment for 30 min. Then, 20 μL of above slurry was coated onto a glassy carbon electrode with a diameter of 5 mm and dried naturally at room temperature.

OER measurements

OER measurements were performed in a three-electrode system using a rotating disk electrode (PINE Research Instrumentation, at a rotation speed of 1500 r.p.m.) and the data were collected by a CHI 760E electrochemical workstation (CH instrument, Shanghai). A Ag/AgCl (KCl, 4 M) electrode and a Pt foil (1*1 cm²) were used as the reference electrode and the counter electrode, respectively. All current densities were normalized to the geometrical surface area and the measured potential vs. Ag/AgCl was converted to the potential vs. the reversible hydrogen electrode (RHE) according to $E(\text{RHE}) = E(\text{Ag/AgCl}) + (0.205 + 0.059 \text{ pH})\text{V}$. Linear sweep voltammetry (LSV) measurements were taken at a scan rate of 2 mV s⁻¹ to obtain the polarization curves, and 1.0 M KOH solution was used as aqueous electrolyte with a continuous flow of O₂ during the test in order to ensure the O₂/H₂O equilibrium at 1.23 V vs. RHE. The Tafel slope was calculated according to Tafel equation $\eta = b \cdot \log(j/j_0)$ (η is the overpotential, b is Tafel slope, j is the current density, and j_0 is the exchange current density). Overpotential was calculated by $\eta = E$ (vs. RHE) - 1.23, considering O₂/H₂O equilibrium at 1.23 V vs. RHE.

In order to investigate the electrocatalytic oxygen evolution mechanism, the rotating ring-disk electrode (RRDE) voltammograms were conducted on a RRDE configuration (Pine Research Instrumentation, USA) composed of a disk electrode (glassy carbon) and a ring electrode (platinum). 20 μL of electrocatalyst ink was coated onto the disk electrode, and a scan rate of 2 mV s⁻¹ was utilized for RRDE experiments with a rotation rate of 1500 r.p.m.. In order to determine the reaction pathway for OER by detecting the HO²⁻ formation, the ring potential was held constantly at 1.50 V vs. RHE to oxidize possible HO²⁻ intermediate in O₂-saturated KOH aqueous solution during the OER process. Next, a continuous OER (disk electrode) to ORR (ring electrode) process occurring on the RRDE was used to confirm that the

observed anodic current originates from the OER process, rather than other side reactions and meanwhile to further collect the Faradaic efficiency. The ring potential of the RRDE was kept constantly at 0.4 V vs. RHE to reduce the O₂ produced from catalyst on the disk electrode in N₂-saturated electrolyte. [See Ma, T. Y.; et. al., *J. Am. Chem. Soc.* 2014, **136**, 13925–13931, and Zhu, Y. P.; et. al., *Adv. Funct. Mater.* 2015, **25**, 7337–7347.] And, the Faradaic efficiency (ϵ) was calculated based on the following equation: $\epsilon = \text{Ir}/(\text{IdN})$, where Id and Ir stand for the disk current and the ring current, respectively, and N represents the current collection efficiency of RRDE. Furthermore, IrO₂ is a well-established benchmark OER catalyst with almost 100% Faradaic efficiency because it is free of probable carbon oxidation during the OER process, and therefore IrO₂ thin-film electrode is selected for the calibration of the collection efficiency of the RRDE. [see T. Nakagawa, et. al., *J. Am. Chem. Soc.* 2009, **131**, 15578–15579] Thus, the N value is determined to be 0.2. To collect the Faradaic efficiency, the disk electrode current was held at a small constant current of 200 μA, which is large enough to ensure an appreciable O₂ production and sufficiently small to minimize local saturation and bubble formation at the disk electrode. [see C. C. L. McCrory, et. al., *J. Am. Chem. Soc.* 2013, **135**, 16977–16987]

The long-term stability test was performed by i-t curve at a certain potential for 12 h using a rotating speed of 1500 r.p.m.. To evaluate the electrochemical double-layer capacitance (ECSA), cyclic voltammograms (CVs) were tested from 1.15 to 1.19 V (vs. RHE, in 1.0 M KOH) with scan rates ranging from 20 to 60 mV s⁻¹. Electrochemical impedance spectroscopy (EIS) was performed at potential of 1.6 V vs. RHE with frequencies from 500,000 to 1 Hz with an amplitude of 5 mV. All the data presented were not corrected for iR losses.

HER measurements

For HER measurements, the typical process is similar to that of OER, in which a flow of N₂ instead of a flow of O₂ was maintained over the electrolyte over the entire electrochemical tests to ensure the H₂/H₂O equilibrium at 0 V vs. RHE.

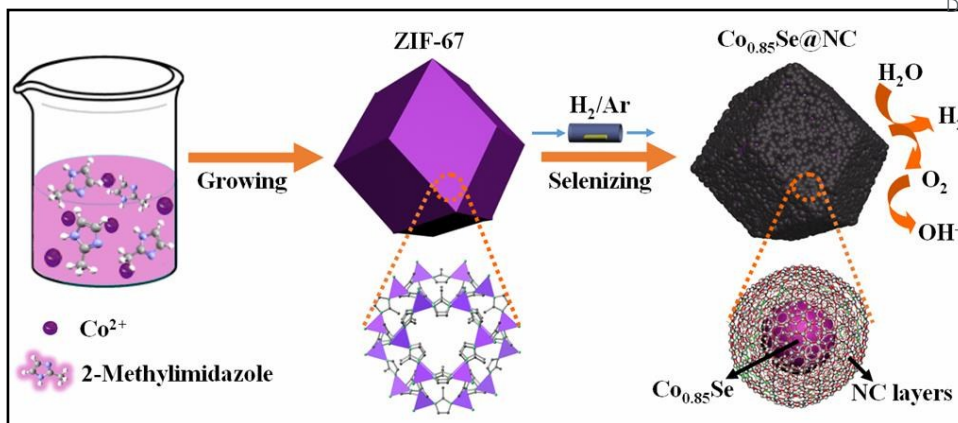
Overall water splitting

To evaluate the full water electrolysis, the Co_{0.85}Se@NC catalyst coated onto nickel foam substrate was used as both anode and cathode. The electrolyte was purged with N₂ gas for 30 min under ambient condition before the electrochemical tests.

ORR measurements

For ORR measurements, the typical strategy is similar to that of OER. The electrochemical experiments were carried out in O₂-saturated 0.1 M KOH electrolyte for the ORR. The potential range is cyclically scanned between 0.172 and 1.172 V vs. RHE with a scan rate of 10 mV s⁻¹. The CV and LSV were obtained at ambient temperature after purging O₂ or N₂ gas for 30 min. The potential cycling was repeated until the stable voltammogram curves were obtained.

RDE measurements were carried out at rotating rates varying from 400 to 2025 r.p.m. at a scan rate of 10 mV s⁻¹. The kinetic parameters can be obtained on the basis of Koutecky-Levich equations as follows:



Scheme 1 Illustration of the fabrication procedure for $\text{Co}_{0.85}\text{Se}@\text{NC}$.

$$1/J = 1/J_k + 1/(B\omega^{1/2})$$

$$B = 0.2nFC_0D_0^{2/3}\nu^{-1/6}$$

$$J_k = nFkC_0$$

Where J is the measured current density, J_k is the kinetic current density, ω is the rotation speed (the constant 0.2 is used when the rotation speed is expressed in rpm), n is the transferred electron number, F is the Faraday constant (96485 C mol^{-1}), C_0 is the saturated concentration of O_2 in the electrolyte ($1.21 \times 10^{-3} \text{ mol L}^{-1}$), D_0 is the diffusion coefficient of O_2 in the solution ($1.9 \times 10^{-5} \text{ cm}^2 \text{ s}^{-1}$), ν is the kinetic viscosity of the electrolyte ($0.01 \text{ cm}^2 \text{ s}^{-1}$), and k is the electron-transfer rate constant.

Zn-air batteries

The rechargeable Zn-air batteries were tested in home-made electrochemical cells, and the prepared $\text{Co}_{0.85}\text{Se}@\text{NC}$ was coated on carbon paper substrate as the air cathode, a polished Zn plate was applied as the anode, and a 6 M KOH + 0.2 M $\text{Zn}(\text{Ac})_2$ aqueous solution was utilized as the electrolyte. Battery tests were performed at room temperature on a LAND CT2001A instrument. For the cycling test, one cycle consists of one discharging step (10 mA cm^{-2} for 5 min) followed by one charging step of the same current density and duration time.

Results and discussion

The overall fabrication process of $\text{Co}_{0.85}\text{Se}@\text{NC}$ is schematically illustrated in Scheme 1 (details see Experiment Section). First, ZIF-67 was prepared by a facile and scalable method. $\text{Co}(\text{NO}_3)_2 \cdot 6\text{H}_2\text{O}$ and 2-methyl-imidazole were mixed in ethanol solvent under magnetic stirring at ambient temperature and after 24 h, ZIF-67 was formed (Fig. S1a). Subsequently, ZIF-67 and Se powder with an appreciate mass ratio were put in two separate positions of a porcelain boat. Then the porcelain boat was put into a furnace with Se powder at the upstream side of the furnace and heated at appropriate temperature under H_2/Ar atmosphere. During the heat treatment process, the organic ligand of 2-methyl-imidazole in ZIF-67 was carbonized into N-doped carbon and simultaneously Co existing in ZIF-67 was selenized into $\text{Co}_{0.85}\text{Se}$ surrounded by *in situ* formed N-doped carbon, thus leading to the formation of

$\text{Co}_{0.85}\text{Se}@\text{NC}$. The phase composition of the resultant sample was first characterized by X-ray diffraction (XRD). As shown in Fig. 1a, the main diffraction peaks at 33.3° , 44.7° , 50.6° , 60.4° , 61.7° and 69.9° , can be assigned to (101), (102), (110), (103), (112), and (202) planes of hexagonal $\text{Co}_{0.85}\text{Se}$ (JCPDS, No. 52-1008), respectively, indicating that $\text{Co}_{0.85}\text{Se}$ alloy phase has been successfully synthesized by the current strategy. That broad peak in the 2θ range of 20° – 30° is related to carbon species, which is further confirmed by Raman spectroscopy. From Fig. 1b, we can see that two prominent peaks at around 1341.5 and 1586.9 cm^{-1} are clearly observed, and they are assigned to the D and G bands of carbon, respectively. The D band is related to the structural defects or partially disordered structures in carbon materials, while the G band is associated with the degree of graphitization. The carbon species in $\text{Co}_{0.85}\text{Se}@\text{NC}$ is determined to be around 31 wt% from thermogravimetric analysis (TG) curve (Fig. 1c). Furthermore, X-ray photoelectron spectroscopy (XPS) is performed to further analyze the surface chemical information of $\text{Co}_{0.85}\text{Se}@\text{NC}$. The survey XPS spectrum in Fig. S2 confirms Se, C, N, O, and Co elements existing in $\text{Co}_{0.85}\text{Se}@\text{NC}$. The presence of the O element is probably due to the absorbed oxygen-species or the oxidized parts caused by being exposed in air. Fig. 1d shows high resolution C 1s XPS spectrum, which can be deconvoluted into three peaks centered at 284.6, 285.6, and 288.7 eV, corresponding to C–C, C=N, and O–C=O bonds, respectively. High resolution Co 2p XPS spectrum (Fig. 1e) shows the peaks of Co $2\text{P}_{3/2}$ and Co $2\text{P}_{1/2}$ with binding energies at 780.0 and 796.6 eV as well as two satellite peaks at 785.8 and 803.0 eV. Co $2\text{P}_{3/2}$ peak can be deconvoluted into four components with binding energies at 777.8, 779.4, 780.3, and 781.6 eV, corresponding to Co^0 , Co^{2+} , Co–N_x, and Co^{3+} , respectively.^{31,37–39} The Co^{2+} and Co^{3+} may result from the surface oxidation under ambient air, consistent with the reported result.²⁷ Fig. 1f shows high resolution Se 3d XPS spectrum, in which Se $3\text{d}_{5/2}$ and $3\text{d}_{3/2}$ peaks at 53.6 and 54.2 eV with a spin-orbit splitting of 0.86 eV can be assigned to Se^0 , while that wide and weak peak at about 59.7 eV discloses the presence of SeO_x .^{15,30} Furthermore, high resolution N 1s XPS spectrum (Fig. 1g) can be deconvoluted into

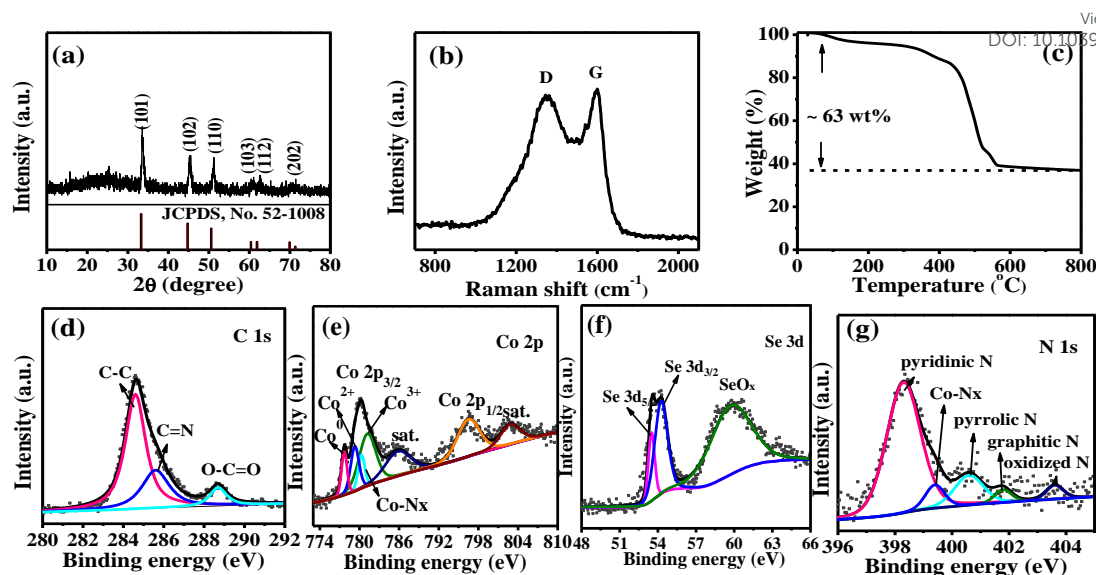


Fig. 1 (a) XRD pattern, (b) Raman spectrum and (c) TG curve of $\text{Co}_{0.85}\text{Se}@NC$; High-resolution XPS spectra of (d) C 1s, (e) Co 2p, (f) Se 3d, and (g) N 1s for $\text{Co}_{0.85}\text{Se}@NC$.

five components with binding energies at 398.2, 403.7, 400.6, 401.8, and 403.7 eV, which can be assigned to pyridinic N, Co-N_x, pyrrolic N, graphitic N, and oxidized N, respectively.^{39,40} And total nitrogen content in $\text{Co}_{0.85}\text{Se}@NC$ is determined to be as high as 5.26 wt% by CHN element analysis. These XPS results confirm the surface chemical states of all elements involved in $\text{Co}_{0.85}\text{Se}@NC$ as well as the formation of Co-N-C. If the original mass ratios of ZIF-67 to Se powder were 1:2 and 1:0, $\text{CoSe}_2@NC$ and $\text{Co}@NC$ were obtained, respectively (Fig. S3).

More information about the charge states and electronic nature of $\text{Co}_{0.85}\text{Se}@NC$ was obtained from X-ray adsorption near-edge structure (XANES) and extended X-ray absorption fine structure (EXAFS) analysis. As shown in Fig. 2a, the pre-edge of Co K-edge XANES spectrum of $\text{Co}_{0.85}\text{Se}@NC$ clearly shifts towards the higher energy compared to that of pristine $\text{Co}_{0.85}\text{Se}$, indicating the existence of strong interaction between $\text{Co}_{0.85}\text{Se}$ and N-doped carbon, which is caused by a negative charge-transfer from Co to carbon.^{41,42} Furthermore, Fig. 2b shows the Fourier transformed k^3 -weighted EXAFS data for $\text{Co}_{0.85}\text{Se}@NC$ and $\text{Co}_{0.85}\text{Se}$. Clearly, $\text{Co}_{0.85}\text{Se}@NC$ exhibits a relatively strong peak at 1.56 Å, which can be assigned to typical Co-N bond.^{41,43} This result further confirms the

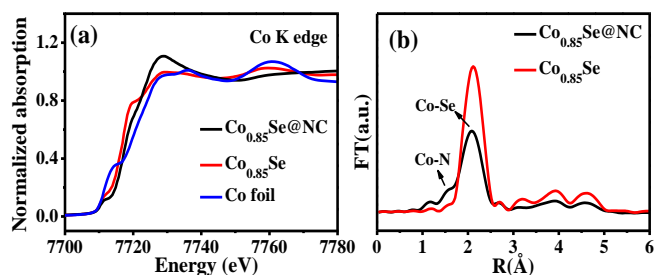


Fig. 2 (a) Co K-edge XANES spectra for $\text{Co}_{0.85}\text{Se}@NC$, $\text{Co}_{0.85}\text{Se}$, and Co foil. (b) Fourier transformed k^3 -weighted EXAFS spectra for $\text{Co}_{0.85}\text{Se}@NC$ and $\text{Co}_{0.85}\text{Se}$.

existence of the Co-N_x bond in $\text{Co}_{0.85}\text{Se}@NC$, which is constructed by the interaction between $\text{Co}_{0.85}\text{Se}$ and N-doped carbon, in well agreement with above XPS results. It has been well addressed that the Co-N_x bond is beneficial for improving the electrocatalytic activity of the materials.³²

Fig. 3a shows a representative field emission scanning electron microscopy (FE-SEM) image of $\text{Co}_{0.85}\text{Se}@NC$. It can be clearly seen that the sample completely inherits the polyhedral morphology of the ZIF-67 precursor (Fig. S1b, Supporting information). Compared to ZIF-67 polyhedrons with a fairly smooth surface, the $\text{Co}_{0.85}\text{Se}@NC$ polyhedrons are much rougher in surface and have a length of 200 nm. During the thermal treatment process, a full phase transformation occurs from ZIF-67 to $\text{Co}_{0.85}\text{Se}@NC$, which is the reason for the formation of the rougher surface. The microstructure of $\text{Co}_{0.85}\text{Se}@NC$ is further investigated by transmission electron microscopy (TEM). As depicted in Fig. 3b, the polyhedral structure is also observed, same as above FE-SEM result. A detailed examination for a single polyhedron (Fig. 3c) reveals that the $\text{Co}_{0.85}\text{Se}@NC$ polyhedron is composed of numerous small nanocrystals. Besides, a highly porous texture can be clearly observed throughout the whole polyhedron, which may result from the decomposition of organic species in ZIF-67 during the thermal treatment process. More details on the edge of $\text{Co}_{0.85}\text{Se}@NC$ polyhedron can be obtained from Fig. 3d. Numerous 10 nm-sized $\text{Co}_{0.85}\text{Se}$ nanocrystals (darker areas indicated by red circles) are embedded in carbon matrix (as verified by Raman, TG and XPS), which may play important roles in prohibiting the further growth of the $\text{Co}_{0.85}\text{Se}$ nanocrystals, stabilizing the polyhedral structure, and affecting the electronic structure of Co. Furthermore, a representative high-resolution TEM (HRTEM) image (Fig. 3e) clearly shows that a carbon layer with a thickness of about 1–2 nm is formed on the surface of a $\text{Co}_{0.85}\text{Se}$ nanocrystalline, which results from *in situ* carbonizing of the organic ligand in ZIF-67. The

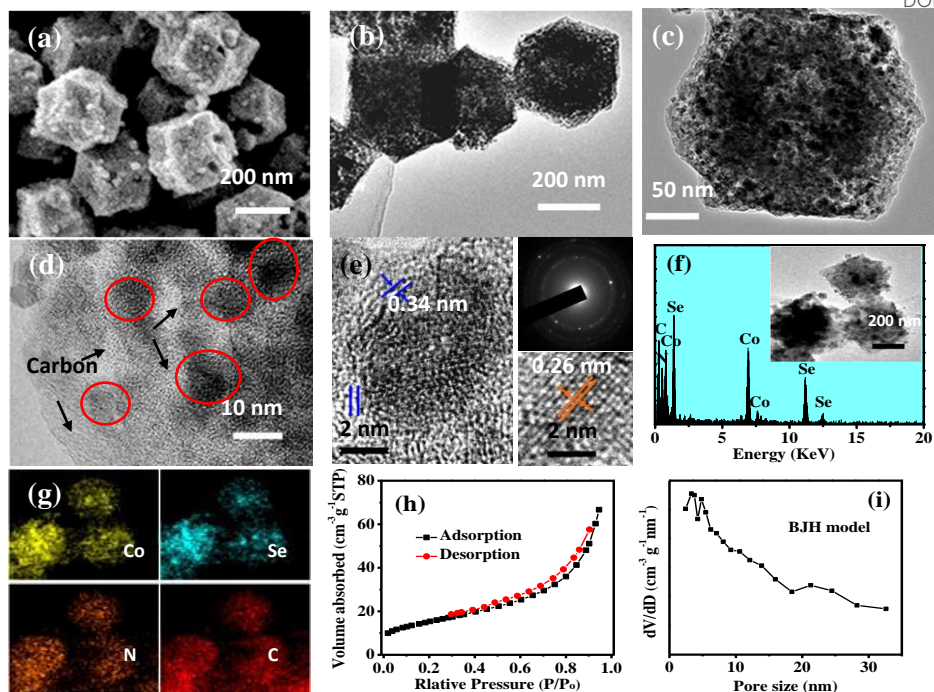


Fig. 3 (a) FE-SEM image, (b–d) TEM images, (e) HRTEM image and SAED pattern of $\text{Co}_{0.85}\text{Se}@NC$. (f) EDS spectrum and scanning transmission electron microscopy (STEM) image, and (g) corresponding element mappings of $\text{Co}_{0.85}\text{Se}@NC$. (h) N_2 adsorption–desorption isotherms of $\text{Co}_{0.85}\text{Se}@NC$ and (i) corresponding pore size distribution curve from the BJH model.

resolved interplanar distances of the lattice fringes are 0.26 and 0.34 nm, corresponding to the (101) planes of $\text{Co}_{0.85}\text{Se}^{16}$ and the (001) planes of graphite, respectively. The selected-area electron diffraction (SAED) pattern also confirms the polycrystalline nature of the $\text{Co}_{0.85}\text{Se}$ nanocrystals. Additionally, in agreement with the results from XPS measurements, the energy-dispersive spectroscopy (EDS) spectrum also confirms that the $\text{Co}_{0.85}\text{Se}@NC$ samples is composed of Co, Se, C, and N elements (Fig. 3f), and that these elements are homogeneously distributed (Fig. 3g). Moreover, the N_2 adsorption isotherms recorded on $\text{Co}_{0.85}\text{Se}@NC$ belong to type IV with a hysteresis loop of type H4 (Fig. 3h), which is usually observed for mesoporous materials with slit-like pores, in good agreement with above TEM observations. Correspondingly, the sizes of the mesopores are mainly in the range of 2–20 nm from the pore size distribution curve (Fig. 3i). Also, $\text{Co}_{0.85}\text{Se}@NC$ displays a high specific Brunauer–Emmett–Teller (BET) surface area of $55 \text{ m}^2 \text{ g}^{-1}$. The rich porous channel and high surface area of $\text{Co}_{0.85}\text{Se}@NC$ may result from the porous structure of the ZIF-67 template, and at the same time they are beneficial for improving its electrocatalytic performance.

The electrocatalytic OER activity of $\text{Co}_{0.85}\text{Se}@NC$ was first evaluated by the polarization linear sweep voltammograms (LSVs) recorded in O_2 -saturated 1.0 M KOH aqueous solution with a scan rate of 2 mV s^{-1} using a standard three-electrode configuration (see Experimental section for details). For comparison, $\text{CoSe}_2@NC$, $\text{Co}@NC$, $\text{Co}_{0.85}\text{Se}$ (Fig. S4), NC (Fig. S5), ZIF-67, Pt/C, and IrO_2/C were also tested at the same conditions. The $\text{Co}_{0.85}\text{Se}@NC$ exhibits the optimal performance

with a mass loading of 0.4 mg cm^{-2} on a glassy carbon (GC) disk electrode (Fig. S6a), while the catalysts prepared with lower or higher temperatures show slightly inferior OER performance (Fig. S6b), and therefore in the following discuss, we compare this optimal result with those of other samples. First, as shown in Fig. S3b, the OER activity of $\text{Co}_{0.85}\text{Se}@NC$ is obviously better than those of $\text{Co}@NC$ and $\text{CoSe}_2@NC$. As we know, the Co–Se bond can lead to the Co in $\text{Co}_{0.85}\text{Se}@NC$ with a high valence state,^{30,44} and this is able to boost the OER adsorption process, which can be further supported by its Tafel slop value (Fig. S3c) ($75 \text{ vs. } 101 \text{ mV dec}^{-1}$ for $\text{Co}_{0.85}\text{Se}@NC \text{ vs. } \text{Co}@NC$). In addition, $\text{Co}_{0.85}\text{Se}@NC$ has a higher Co/Se atomic ratio than $\text{CoSe}_2@NC$, and this can enhance the adsorption process in OER reaction as $\text{Co}_{0.85}\text{Se}@NC$ has a small Tafel slop value (Fig. S3c), which is determined by its inherent phase structure, commonly observed in other works.^{44,45} Moreover, the NC and ZIF-67 show negligible current densities below the potential of 1.60 V vs. reversible hydrogen electrode (RHE), while the pristine $\text{Co}_{0.85}\text{Se}$ presents the OER response with an onset potential at 1.59 V (Fig. 4a), indicating that the catalytic sites come mainly from $\text{Co}_{0.85}\text{Se}$. In contrast, the $\text{Co}_{0.85}\text{Se}@NC$ exhibits significantly enhanced OER catalytic activity. Specifically, the $\text{Co}_{0.85}\text{Se}@NC$ reveals a sharp onset of OER current at approximately 1.49 V, indicating that the synergistic effect between $\text{Co}_{0.85}\text{Se}$ and NC is responsible for the excellent OER performance. Noticeably, although the IrO_2/C affords a onset potential of approximately 1.47 V, slightly smaller than that of $\text{Co}_{0.85}\text{Se}@NC$, its OER current densities drop obviously

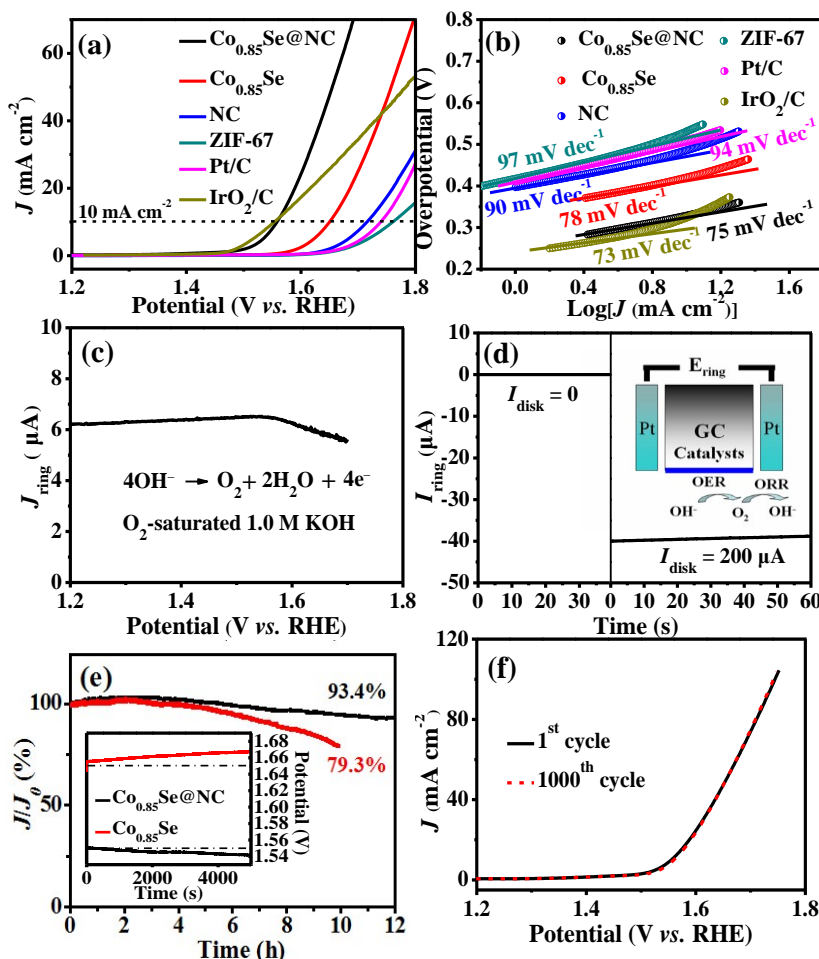


Fig. 4 (a) Polarization curves and (b) Tafel plots of $\text{Co}_{0.85}\text{Se@NC}$, $\text{Co}_{0.85}\text{Se}$, NC, ZIF-67, Pt/C, and IrO_2/C in an O_2 -saturated 1.0 M KOH solution (scan rate of 2 mV s^{-1}). (c) The ring current of $\text{Co}_{0.85}\text{Se@NC}$ on a RRDE (1500 r.p.m.) in O_2 -saturated 1.0 M KOH solution (ring potential: 1.50 V vs. RHE). (d) The ring current of $\text{Co}_{0.85}\text{Se@NC}$ on a RRDE (1500 r.p.m.) in N_2 -saturated 1.0 M KOH solution (ring potential: 0.40 V vs. RHE). (e) Chronoamperometric response at a constant potential (the potential at 10.0 mA cm^{-2}), and the inset in (e) shows the chronopotentiometric response of $\text{Co}_{0.85}\text{Se@NC}$ and $\text{Co}_{0.85}\text{Se}$ at 10.0 mA cm^{-2} . (f) Polarization curves of $\text{Co}_{0.85}\text{Se@NC}$ before and after 1000 cycles.

below those of $\text{Co}_{0.85}\text{Se@NC}$ at high bases, indicating the excellent OER catalytic activity of the $\text{Co}_{0.85}\text{Se@NC}$. Moreover, we further compared the operating potentials required for all the catalysts to deliver the 10.0 mA cm^{-2} current density, the approximate current density expected for a 10% efficient solar water-splitting device under 1 sun illumination.^{46,47} The operating potential of $\text{Co}_{0.85}\text{Se@NC}$ at the current density of 10 mA cm^{-2} is 1.55 V, comparable to that of the state-of-the-art IrO_2/C catalyst (1.55 V), but much lower than those of $\text{Co}_{0.85}\text{Se}$ (1.65 V), NC (1.72 V), ZIF-67 (1.76 V), Pt/C (1.74 V), CoSe_2/NC (1.64 V), Co@NC (1.69 V), and many other reported catalysts, for example, IrO_2/C (1.60 V, 0.1 M KOH),⁴⁸ Pt/C (1.83 V, 0.1 M KOH),⁴⁹ CoSe_2 ultrathin nanosheets (1.55 V, 0.1 M KOH),¹² CoSe_2/N -graphene (1.596 V, 0.1 M KOH),⁵⁰ $\text{Mn}_3\text{O}_4/\text{CoSe}_2$ hybrids (1.68 V, 0.1 M KOH),¹¹ $\text{CoS}_2/\text{N,S-GO}$ (1.61 V, 0.1 M KOH),⁵¹ and TCCN (1.65 V, 0.1 M KOH).³² A detailed comparison of various OER catalysts reported recently is presented in Table S1, further confirming the outstanding catalytic activity of the $\text{Co}_{0.85}\text{Se@NC}$. The OER kinetics of the above catalysts were further examined by Tafel plots, as shown

in Fig. 4b. The Tafel slopes are found to be 75, 88, 90, 97, 94, and 73 mV dec^{-1} for $\text{Co}_{0.85}\text{Se@NC}$, $\text{Co}_{0.85}\text{Se}$, NC, ZIF-67, Pt/C, and IrO_2/C , respectively. Clearly, the Tafel slope of $\text{Co}_{0.85}\text{Se@NC}$ is close to that of the IrO_2/C , but it is lower than those of the control samples and some of the previously reported OER catalysts (Table S1). This result suggests that the $\text{Co}_{0.85}\text{Se@NC}$ has a favorable OER reaction kinetics corresponding to its high catalytic activity.

To obtain further insights into the reaction mechanism, we used the rotating ring-disk electrode (RRDE) technique with a Pt ring electrode potential of 1.50 V to oxidize the peroxide intermediates formed on the $\text{Co}_{0.85}\text{Se@NC}$ surface during the OER process. As shown in Fig. 4c, it can be clearly seen that a fairly low ring current of $6 \mu\text{A}$ is detected and this value is 3 orders of magnitude lower than that of the disk current (mA scale), which is so small that it can be negligible. So it can be reasonably concluded that $\text{Co}_{0.85}\text{Se@NC}$ favors a desirable four-electron pathway for water oxidation ($4\text{OH}^- \rightarrow \text{O}_2 + 2\text{H}_2\text{O} + 4\text{e}^-$). Moreover, in order to prove that the observed anodic current results from the OER process rather than other side

reactions and also to further collect the Faradaic efficiency, a RRDE with a ring electrode potential of 0.40 V (a value to ensure that the ORR can be taken place) in N₂-saturated medium was employed to reduce the generated O₂ from the OER process (Fig. 4d), thus guaranteeing a continuous OER (disk electrode) to ORR (ring electrode) process (the inset of Fig. 3d).^{3,44} When the disk current was fixed at 200 μ A, a constant ring current of about 39 μ A (collection efficiency 0.2) can be detected, indicating that the anodic current catalyzed by Co_{0.85}Se@NC is attributed to the OER process with a high Faradaic efficiency of 97.5%.^{10,51}

Another critical criterion for evaluating the OER performance of the electrocatalysts is the long-term durability, which is significant for energy conversion and storage systems. As shown in Fig. 4e, the chronoamperometric response curve for Co_{0.85}Se@NC at a low potential of 1.55 V exhibits an anodic current attenuation as small as 6.6% within 12 h, demonstrating a high stability. This insignificant activity decrease of Co_{0.85}Se@NC may be caused by a small amount of the Co_{0.85}Se@NC catalyst peeling off the electrode during the evolution of a large amount of O₂ gas for the long process.⁴⁵ In contrast, Co_{0.85}Se displays not only 3.1 times larger current attenuation (20.7%) than Co_{0.85}Se@NC, but also 100 mV larger potential to afford the same current density response within 10 h (Fig. S7), indicating the synergistic effect between Co_{0.85}Se and NC. The TEM image of the Co_{0.85}Se@NC electrocatalyst after a 12 h reaction shows a good polyhedron structure, almost completely same as that of the fresh Co_{0.85}Se@NC (Fig. S8a). Besides, the HRTEM image gives the interplanar distance of the lattice fringes to be 0.26 nm, which corresponds to the (101) planes for Co_{0.85}Se (Fig. S8b), suggesting the fact that the Co_{0.85}Se phase does not change during the OER process. All of

these findings indicate the superior stability and excellent OER catalytic activity of Co_{0.85}Se@NC. Furthermore, from the chronopotentiometric curve tested at the current density of 10.0 mA cm⁻² (the inset in Fig. 4e), we can see that Co_{0.85}Se@NC holds a nearly constant operating potential at 1.55 V with a trend of continuous potential decrease corresponding to its current increase in *i*-*t* curve in the first 3 h, which is owing to the spread of the electrolyte, while the potential of Co_{0.85}Se increases about 13 mV from 1.650 to 1.663 V as a striking contrast within 5000 s, again revealing the superior durability of Co_{0.85}Se@NC. Additionally, accelerated degradation studies are carried out by taking continuous cyclic voltammograms (CVs) at an accelerated sweep rate of 50 mV s⁻¹ for 1000 cycles to probe the stability of the catalyst, only 2.6% anodic current loss (4 mV increased) is observed for Co_{0.85}Se@NC, further confirming its highly stable performance (Fig. 4f).

The outstanding OER performance of Co_{0.85}Se@NC originates from the synergistic effect between ultrafine Co_{0.85}Se nanocrystals and highly conductive N-doped carbon, the Co-N-C structure constructed by the interaction between the high content N and Co_{0.85}Se species, and unique porous architecture. Firstly, the synergistic effect between the highly conductive N-doped carbon and ultrafine Co_{0.85}Se plays an important role in enhancing the OER performance of Co_{0.85}Se@NC. As discussed above, the pre-edge of Co K-edge XANES spectrum of Co_{0.85}Se@NC (Fig. 2a) has shifted towards the higher energy compared to Co_{0.85}Se due to negative charge transfer from Co to carbon,^{41,42} indicating strongly coupling effect between Co_{0.85}Se nanocrystals and N-doped carbon species. And, the *in situ* incorporated N-doped carbon causes the impaired electron density of Co atoms, which can make the electro-catalytically active sites of Co more electrophilic,^{42,53}

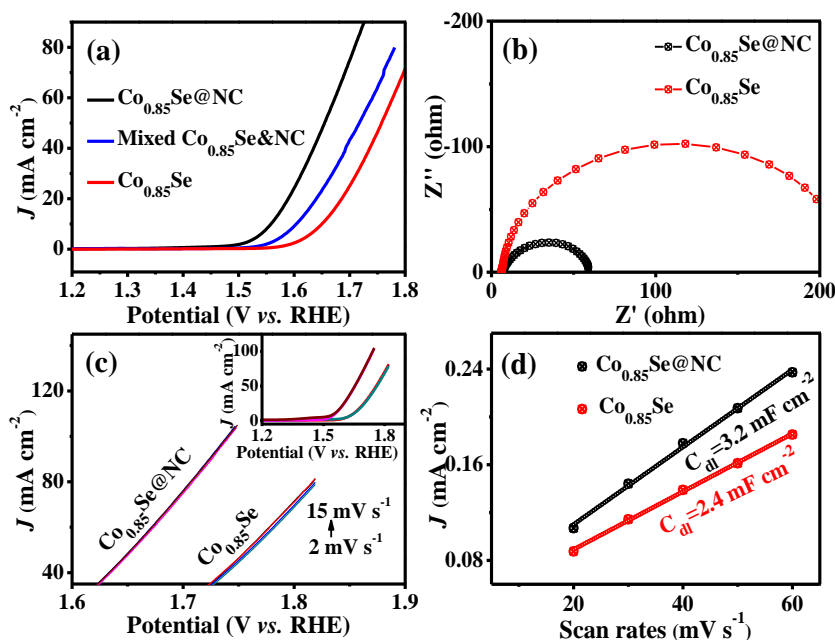


Fig. 5 (a) Polarization curves of Co_{0.85}Se@NC, physically mixed Co_{0.85}Se with NC, and Co_{0.85}Se. (b) EIS of Co_{0.85}Se@NC and Co_{0.85}Se tested at 1.60 V vs. RHE. (c) Polarization curves of Co_{0.85}Se@NC and Co_{0.85}Se at different scan rates. (d) Plots of the current density at 1.17 V (V vs. RHE) vs. the scan rate of Co_{0.85}Se@NC and Co_{0.85}Se.

electro-catalytically active sites of Co more electrophilic,^{42,53} thus facilitating the adsorption and reaction of OH⁻ groups with Co_{0.85}Se@NC,⁵⁴ resulting in outstanding OER performance. Besides, the *in situ* uniformly anchoring of Co_{0.85}Se on the N-doped carbon, assured by the use of the ZIF-67 as the precursor, can greatly improve the conductivity and charge transfer capability of the Co_{0.85}Se catalyst. The strong coupling effect between them can take full advantage of the superior electric conductivity of the N-doped carbon backbone, which can facilitate the charge transfer in the hybrid catalyst, thus resulting in an enhanced OER activity and stability. For instance, compared to the physically mixed Co_{0.85}Se and NC, and carbon-free Co_{0.85}Se, Co_{0.85}Se@NC has a smaller onset potential with continually enhanced current density, suggesting its much higher OER activity (Fig. 5a). Moreover, Co_{0.85}Se@NC has a smaller semicircular diameter in the electrochemical impedance spectroscopy (EIS) than Co_{0.85}Se

(Fig. 5b), revealing its smaller contact impedance and faster charge transport along with favorable reaction kinetics. The higher OER electrocatalytic activity and smaller charge transfer impedance of Co_{0.85}Se@NC both benefit from the strong coupling between Co_{0.85}Se and N-doped carbon. Additionally, N-doped carbon matrix might also play an important role in prohibiting the growth of Co_{0.85}Se nanocrystals, thus increasing the catalytic sites and stabilizing the polyhedral structure of Co_{0.85}Se@NC to contribute microstructure effect such as the porous structure.

Secondly, the N content of Co_{0.85}Se@NC can be achieved as high as 5.26 wt% determined by CHN elemental analysis. Such a high N content not only can directly act as OER active sites but also can incorporate with metals (e.g. Co species) forming Co-N-C structure (as proofed by XPS and XANES) to boost the OER performance. Recently, Qiao³² reported that Ti-N_x motifs constructed by interacting between carbon nitride and

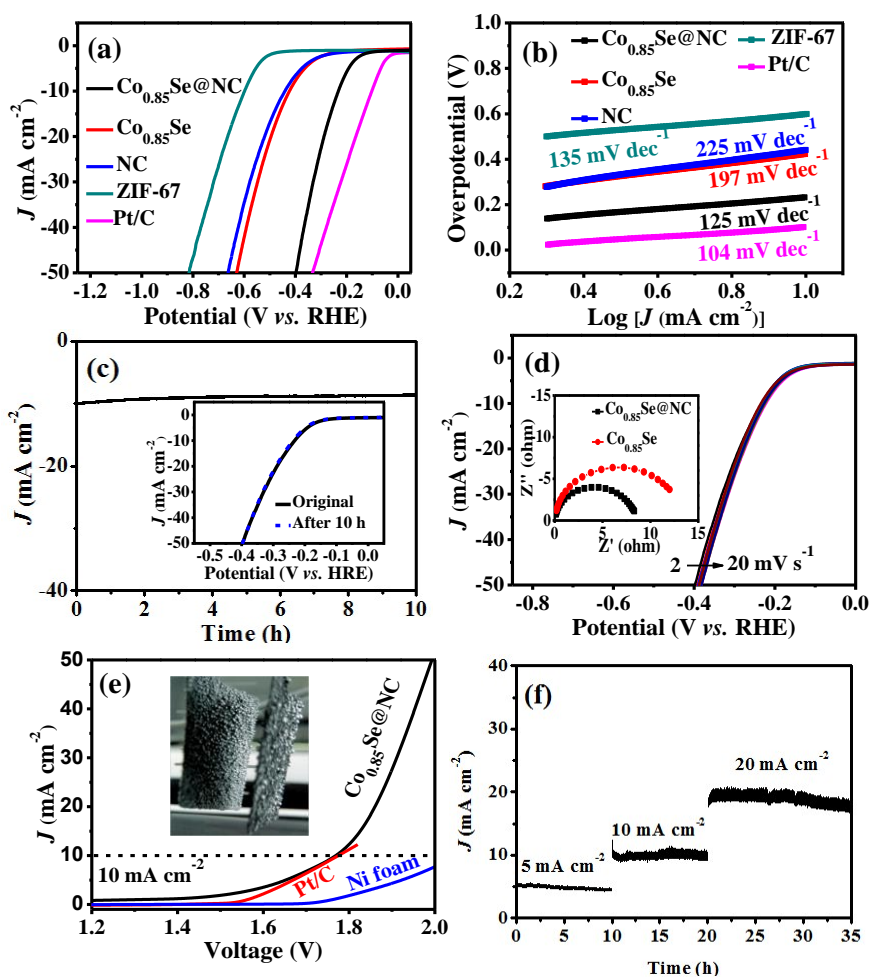


Fig. 6 (a) Polarization curves and (b) Tafel plots of Co_{0.85}Se@NC, Co_{0.85}Se, NC, ZIF-67, and Pt/C for HER (N₂-saturated 1.0 M KOH solution with scan rate of 2 mV s⁻¹). (c) Chronoamperometric response at a constant potential of -0.23 V vs. RHE, and inset in (c) shows polarization curves at 2 mV s⁻¹ before and after 10 h chronoamperometric tests. (d) Polarization curves of Co_{0.85}Se@NC tested at scan rates ranging from 2 to 20 mV s⁻¹, and inset of (d) shows the EIS tested at potential of -0.25 V vs. RHE for Co_{0.85}Se@NC and Co_{0.85}Se. (e) Polarization curves of a two-electrode alkaline electrolyzer using Co_{0.85}Se@NC//Co_{0.85}Se@NC, Pt/C//Pt/C and Ni foam//Ni foam as both cathode and anode at a scan rate of 2 mV s⁻¹ in 1.0 M N₂-saturated KOH. (f) Galvanostatic water electrolysis at a series current densities of 5, 10, and 20 mA cm⁻² over the course of 35 h for Co_{0.85}Se@NC//Co_{0.85}Se@NC.

titanium carbide nanosheets can act as OER electroactive sites. Dai³¹ reported that N-doping into both Co₉S₈ and graphene could efficiently enhance electrocatalytic performance for ORR and OER by tuning the electronic properties of Co₉S₈ and graphene. And others also assumed that the metal–N–C structure can boost oxygen electrochemistry performance. Based on these facts, we conjecture that the Co–N–C structure in our case also contributes to increasing the OER performance.

Thirdly, the unique porous architecture of Co_{0.85}Se@NC, on the one hand, can provide abundant and short diffusion pathways for electron/ion transport during the electrochemical reactions, and on the other hand, can afford a large active surface area for increasing catalytic sites. Noticeable, for the OER polarization curves of Co_{0.85}Se@NC, the current density is not susceptible to the scan rate increasing from 2 to 15 mV s⁻¹, while the Co_{0.85}Se acts as a striking contrast (Fig. 5c). This result indicates that the high porosity of Co_{0.85}Se@NC favors the efficient transfer of the electrolyte and the rapid diffusion of the O₂ product. Furthermore, the mesoporous Co_{0.85}Se@NC polyhedrons afford a large active surface area, which has been confirmed by the electrochemical double-layer capacitance (*C_{dl}*) and the calculated slope from the linear relationship of the current density against the scan rate (Fig. S9). Co_{0.85}Se@NC holds a larger *C_{dl}* than Co_{0.85}Se (3.2 vs. 2.4 mF cm⁻²), indicating an enlarged catalytic solid–liquid contact surface area for Co_{0.85}Se@NC (Fig. 5d). Thus, the rich channel and large solid–liquid contact surface area of Co_{0.85}Se@NC provided by its unique porous architecture can obviously increase its OER electrocatalytic performance.

The opposite reaction initiated on the oxygen evolution electrode that can availably catalyze the corresponding cathode hydrogen evolution process as well, is an import figure of merit to pursue bifunctional water electrolysis electrode and simplify the installation. Hence, the catalytic capacity of Co_{0.85}Se@NC for HER is assessed in the identical electrolyte to OER (1.0 M KOH). As shown in Fig. 6a, Co_{0.85}Se@NC holds a small onset potential of around -140 mV at the current density of 2 mA cm⁻² (Fig. S10), beyond which the cathodic current increases rapidly at higher biases, indicating outstanding electrocatalytic activity. The overpotential at the current density of 10 mA cm⁻² for Co_{0.85}Se@NC is 230 mV, which is far smaller than those of Co_{0.85}Se (424 mV), NC (442 mV), ZIF-67 (599 mV), and some other reported non-noble metal HER electrocatalysts. Co_{0.85}Se@NC also possesses a favorable HER reaction kinetics with a small Tafel value of 125 mV dec⁻¹, which is comparable to that of commercial Pt/C (104 mV dec⁻¹), but much smaller than those of Co_{0.85}Se (197 mV dec⁻¹), NC (224 mV dec⁻¹), and ZIF-67 (135 mV dec⁻¹) (Fig. 6b). This result suggests that Co_{0.85}Se@NC has a favorable HER reaction kinetics corresponding to its high catalytic activity. As expected, Co_{0.85}Se@NC performs excellent stability (tested by chronoamperometric model) in basic solution within 10 h only with a minor current drop at the beginning of the HER measurements, which may be due to the loss of the electrocatalyst from the electrode on rapid rotation (Fig. 6c). Furthermore, the polarization curves before and after operating for 10 h in basic medium were also tested (the inset in Fig. 6c),

which show the similar robust durability, indicating the super stability of Co_{0.85}Se@NC. We also studied the relationship between the HER current density and the scan rate. As shown in Fig. 6d, the HER current density for Co_{0.85}Se@NC is not susceptible to the scan rate increasing from 2 to 20 mV s⁻¹. So, the unique porous architecture of Co_{0.85}Se@NC may contribute to the enhanced HER performance. Besides, the synergistic effect between the highly conductive N-doped carbon and ultrafine Co_{0.85}Se also contributes the enhanced HER activity by decreasing the charge transfer impedance (as evidenced by EIS test in the inset of Fig. 6d). Encouraged by the excellent OER and HER performances, we accordingly assembled a water electrolyzer with a two-electrode configuration in 1.0 M KOH, in which the as-synthesized Co_{0.85}Se@NC was coated on Ni foam as both the anode and the cathode (the inset in Fig. 6e). As shown in Fig. 6e, a catalytic current is detected when the applied potential is larger than 1.42 V, and the current density of 10 mA cm⁻² can be gained at a cell voltage of 1.76 V, representing a combined overpotential of 530 mV for full water splitting. And, the overall water splitting performance of Co_{0.85}Se@NC also outperforms those of the commercial Pt/C and the Ni foam substrate. In addition, the stability test indicates that Co_{0.85}Se@NC possesses a high stability with good rate performance as the current density increases from 5 to 10, and 20 mA cm⁻² during 35 h electrocatalysis process (Fig. 6f). The Co_{0.85}Se@NC gives low overpotentials and superior stability, which demonstrates its promising practical application for overall water splitting.

Interestingly, apart from the excellent overall water splitting performance, Co_{0.85}Se@NC also performs a remarkable ORR activity, making it a promising application for metal–air batteries. Specifically, in cyclic voltammograms (CVs, Fig. 7a), one characteristic ORR peak centered at 0.817 V is observed in 0.1 M O₂-saturated KOH solution, showing the electrochemical reduction of oxygen initiated on Co_{0.85}Se@NC, while, in sharp comparison, no significant peak is obtained in N₂-saturated solution. And, this potential (0.817 V) is close to that of the commercial Pt/C catalyst, but far more positive in comparison to those for Co_{0.85}Se (0.617 V), NC (0.73 V), ZIF-67 (0.732 V) (Fig. S11), and previously reported Co-based ORR catalysts (e.g. -0.3 V vs. Ag/AgCl for Co_{0.85}Se/graphene hybrid nanosheets,¹⁶ 0.704 V vs. RHE for N-Co₉S₈/G,³¹ and -0.21 V vs. SCE for Co₃O₄/ON-CNWS⁵⁵), indicating an easier ORR process on Co_{0.85}Se@NC. Accordingly, Co_{0.85}Se@NC displays a sharp onset potential at 0.912 V in the polarization LSVs curves (Fig. 7b), and its limiting current density increases with increasing the rotation speed (e.g. from 400 to 2025 r.p.m.) because of the increased diffusion rate at high speeds.⁵⁶ The corresponding Koutechy–Levich (K–L) plots of Co_{0.85}Se@NC are obtained from LSVs with potentials ranging from 0.272 to 0.572 V vs. RHE (Fig. 7c), and all plots show fairly good linearity, suggesting first-order reaction kinetics toward dissolved oxygen and similar electron–transfer number (*n*) for the ORR process at different potentials. The *n* is calculated to be in the range of 3.98 to 4.03 at the potentials ranging from 0.272 to 0.572 V (Fig. 7d), indicating that the Co_{0.85}Se@NC electrode favors a four-electron oxygen reduction process. Thus,

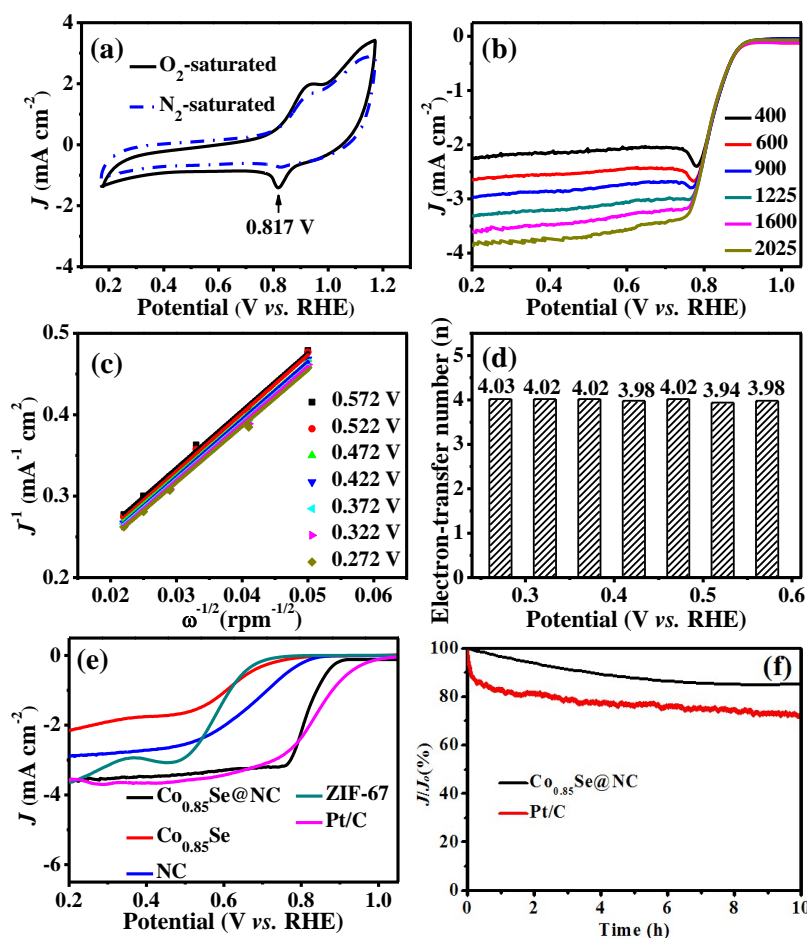


Fig. 7 (a) CVs of the as-synthesized $\text{Co}_{0.85}\text{Se}@NC$ in an O_2 -saturated (black line) or N_2 -saturated (blue dot line) 0.1 M KOH solution (scan rate: 10 mV s^{-1}). (b) Rotating-disk electrode polarization curves (LSVs) of $\text{Co}_{0.85}\text{Se}@NC$ in O_2 -saturated 0.1 M KOH at rotating rates ranging from 400 to 2025 r.p.m. with a scan rate of 10 mV s^{-1} . (c) K–L plots of $\text{Co}_{0.85}\text{Se}@NC$ obtained from the RDE data at 0.572, 0.522, 0.472, 0.422, 0.372, 0.322 and 0.272 V vs. RHE, and (d) the corresponded electron-transfer number. (e) Rotating-disk electrode LSVs of $\text{Co}_{0.85}\text{Se}@NC$, $\text{Co}_{0.85}\text{Se}$, NC, ZIF-67, and Pt/C in O_2 -saturated 0.1 M KOH with a scan rate of 10 mV s^{-1} at 1600 r.p.m. (f) The chronoamperometry curves of $\text{Co}_{0.85}\text{Se}@NC$ and commercial Pt/C catalysts obtained at 0.672 V in O_2 -saturated 0.1 M KOH.

$\text{Co}_{0.85}\text{Se}@NC$ favors a desirable four-electron pathway for reversible OER and ORR process ($4\text{OH}^- \leftrightarrow \text{O}_2 + 2\text{H}_2\text{O} + 4\text{e}^-$), which is of significant importance, especially for rechargeable metal–air batteries and regenerated fuel cells involving these two reactions.

Moreover, we also evaluated the ORR performance of $\text{Co}_{0.85}\text{Se}@NC$, $\text{Co}_{0.85}\text{Se}$, NC, ZIF-67, and commercial Pt/C catalyst using RDE technology at the rotating speed of 1600 r.p.m. in 0.1 M O_2 -saturated KOH (Fig. 7e). Remarkably, $\text{Co}_{0.85}\text{Se}@NC$ displays a significant ORR performance, which is not only better than $\text{Co}_{0.85}\text{Se}$, NC, and ZIF-67 in both the onset potential and the reaction current density, but also comparable to the commercial Pt/C, revealing the high ORR activity of $\text{Co}_{0.85}\text{Se}@NC$. As expected, $\text{Co}_{0.85}\text{Se}@NC$ also shows a strong durability as revealed by the chronoamperometric response (Fig. 7f), retaining 85.2% of the initial current even after 10 h, while the Pt/C catalyst loses 28% of its initial current. The high-activity and good durability of

$\text{Co}_{0.85}\text{Se}@NC$ may be due to the Co–N–C structure, the porous structure and the synergistic effect between the highly conductive N-doped carbon and the ultrafine $\text{Co}_{0.85}\text{Se}$ nanocrystals. These excellent ORR features of $\text{Co}_{0.85}\text{Se}@NC$, especially together with its outstanding OER performance, are particularly desirable for the clean energy systems, such as, rechargeable metal–air batteries and alkaline fuel cells.

Next, proof-to-concept experiments were conducted to demonstrate the potential application of $\text{Co}_{0.85}\text{Se}@NC$ in rechargeable Zn–air batteries since OER and ORR are two fundamental steps in this application. A home-made rechargeable Zn–air battery device was constructed by pairing the zinc plate (the anode), the $\text{Co}_{0.85}\text{Se}@NC$ loaded on carbon fiber paper (the cathode), and O_2 -saturated KOH/ $\text{Zn}(\text{Ac})_2$ electrolyte (Fig. 8a). The battery has an open circuit voltage of $\sim 1.4 \text{ V}$ and a small internal resistance (Fig. S12). Clearly, $\text{Co}_{0.85}\text{Se}@NC$ shows a current density of 186 mA cm^{-2} at a voltage of 1.0 V, which is higher than that of the commercial Pt/C (162 mA cm^{-2}) and other reported values (Table S2). The

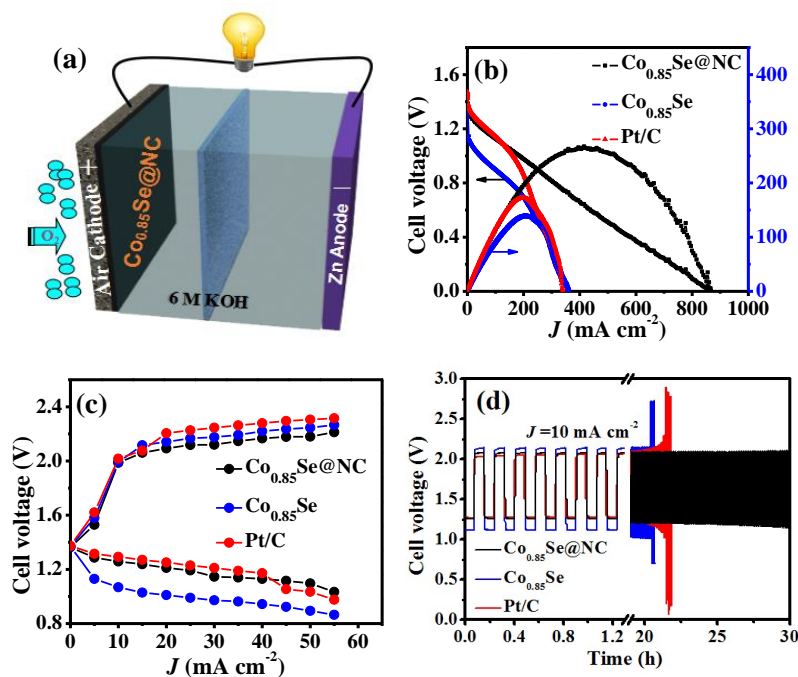


Fig. 8 Electrochemical testing of $\text{Co}_{0.85}\text{Se}@NC$ as the cathode in a home-made Zn–air battery: (a) A schematic of the rechargeable Zn–air battery. (b) A polarization curve ($V\sim i$) and corresponding power density plot of the battery using $\text{Co}_{0.85}\text{Se}@NC$ as the cathode catalyst compared with the primary Zn–air battery using $\text{Co}_{0.85}\text{Se}$ and commercial Pt/C catalyst. (c) Charge and discharge polarization ($V\sim i$) curves of the rechargeable Zn–air battery using $\text{Co}_{0.85}\text{Se}@NC$ compared with the one using $\text{Co}_{0.85}\text{Se}$ and Pt/C (red). (d) Cycling performance of the rechargeable Zn–air battery using $\text{Co}_{0.85}\text{Se}@NC$ at 10 mA cm^{-2} and a 10-min cycle period compared with the one using $\text{Co}_{0.85}\text{Se}$ and commercial Pt/C.

peak power density for $\text{Co}_{0.85}\text{Se}@NC$ (Fig. 8b) is as high as 268 mW cm^{-2} at 0.64 V , which is also superior to those of $\text{Co}_{0.85}\text{Se}$ (139 mW cm^{-2}), Pt/C (173 mW cm^{-2}) and some previously reported materials on Zn–air primary batteries (Table S3). Fig. 8c shows the charge and discharge polarization curves of the rechargeable Zn–air battery using the galvanodynamic method with $\text{Co}_{0.85}\text{Se}@NC$ coated on carbon fiber paper as both the ORR and OER electrodes. It can be clearly observed that $\text{Co}_{0.85}\text{Se}@NC$, $\text{Co}_{0.85}\text{Se}$ and commercial Pt/C all show excellent rate capability during the charging and discharging process. Specifically, $\text{Co}_{0.85}\text{Se}@NC$ shows a discharging potential superior to $\text{Co}_{0.85}\text{Se}$, and comparable to the commercial Pt/C during the ORR process, while for the charging process, $\text{Co}_{0.85}\text{Se}@NC$ obviously outperforms the Pt/C catalyst. And the charge–discharge voltage gap at 20 mA cm^{-2} for $\text{Co}_{0.85}\text{Se}@NC$ is only 0.88 V , which is much smaller than those of $\text{Co}_{0.85}\text{Se}$ (1.13 V) and Pt/C (0.96 V), and some results reported previously (Table S3). Importantly, when repeatedly charged or discharged at 10 mA cm^{-2} with a 10-min per cycle period (including discharging for 5 min, followed by charging the same time) (Fig. 8d), $\text{Co}_{0.85}\text{Se}@NC$ as the air cathode affords a discharge voltage of 1.27 V and a charge voltage of 2.07 V with a small voltage gap of 0.80 V and a high trip efficiency of 61.35% in the first cycle. At the same time, it also shows a high cycling stability with no obvious potential change for over 180 charge–discharge cycles within 30 h, whereas an apparent increase in both the charge and discharge voltages is observed after 120 cycles in 20 h for both $\text{Co}_{0.85}\text{Se}$ and Pt/C. Therefore, the bifunctional $\text{Co}_{0.85}\text{Se}@NC$ electrode is

feasible in practical metal–air batteries with enhanced cyclic stability.

Conclusion

In summary, we have achieved *in situ* coupling of $\text{Co}_{0.85}\text{Se}$ nanocrystals and N-doped carbon via one-step selenizing of metal–organic frameworks. The resultant $\text{Co}_{0.85}\text{Se}@NC$ was used as trifunctional electrocatalysts for overall water splitting and Zn–air batteries for the first time. When used as the electrodes for overall water splitting in alkaline solution, $\text{Co}_{0.85}\text{Se}@NC$ shows a low cell voltage of 1.76 V at the current density of 10 mA cm^{-2} and good stability. At the same time the obtained Zn–air batteries based on $\text{Co}_{0.85}\text{Se}@NC$ exhibit a very low discharge–charge voltage gap (0.80 V at 10 mA cm^{-2}) and long cycle life (up to 180 cycles). Its excellent electrocatalytic performance can be attributed to the synergistic effect of the coupling between $\text{Co}_{0.85}\text{Se}$ and NC, the Co–N–C structure, and the porous conductive carbon network. Our work establishes a facile strategy for the preparation of $\text{Co}_{0.85}\text{Se}@NC$ hybrid as efficient and stable trifunctional electrocatalysts for overall water splitting and Zn–air batteries and this strategy can be extended to fabricate other nanomaterials for energy fields.

Acknowledgements

This work was supported by the National Natural Science Foundation of China (21601014, 21471016 and 21271023) and the 111 Project (B07012). The authors would like to thank the

Analysis & Testing Center of Beijing Institute of Technology for performing FESEM and TEM measurements.

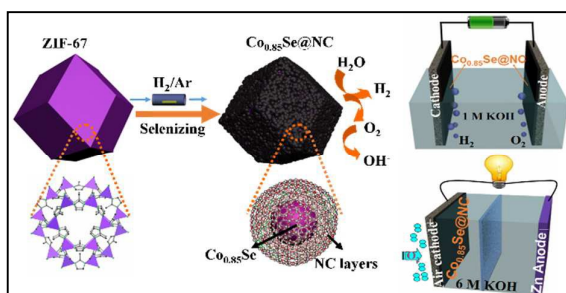
Notes and references

- 1 Y. G. Li, M. Gong, Y. Y. Liang, J. Feng, J. E. Kim, H. L. Wang, G. S. Hong, B. Zhang and H. J. Dai, *Nat. Commun.*, 2013, **4**, 1805–1811.
- 2 H. B. Wu, B. Y. Xia, L. Yu, X. Y. Yu and X. W. D. Lou, *Nat. Commun.*, 2015, **6**, 6512–6519.
- 3 T. Y. Ma, S. Dai, M. Jaroniec and S. Z. Qiao, *J. Am. Chem. Soc.*, 2014, **136**, 13925–13931.
- 4 H. Over, *Chem. Rev.*, 2012, **112**, 3356–3426.
- 5 J. Wang, K. Li, H. X. Zhong, D. Xu, Z. L. Wang, Z. Jiang, Z. J. Wu and X. B. Zhang, *Angew. Chem. Int. Ed.*, 2015, **54**, 10530–10534.
- 6 E. Antolini, *ACS Catalysis*, 2014, **4**, 1426–1440.
- 7 Y. Liang, H. Wang, P. Diao, W. Chang, G. Hong, Y. Li, M. Gong, L. Xie, J. Zhou and J. Wang, *J. Am. Chem. Soc.*, 2012, **134**, 15849–15857.
- 8 S. Peng, L. Li, X. Han, W. Sun, M. Srinivasan, S. G. Mhaisalkar, F. Cheng, Q. Yan, J. Chen and S. Ramakrishna, *Angew. Chem. Int. Ed.*, 2014, **126**, 12802–12807.
- 9 P. Chen, K. Xu, Z. Fang, Y. Tong, J. Wu, X. Lu, X. Peng, H. Ding, C. Wu and Y. Xie, *Angew. Chem. Int. Ed.*, 2015, **127**, 14923–14927.
- 10 Y. P. Zhu, Y. P. Liu, T. Z. Ren and Z. Y. Yuan, *Adv. Funct. Mater.*, 2015, **25**, 7337–7347.
- 11 M. R. Gao, Y. F. Xu, J. Jiang, Y. R. Zheng and S. H. Yu, *J. Am. Chem. Soc.*, 2012, **134**, 2930–2933.
- 12 Y. Liu, H. Cheng, M. Lyu, S. Fan, Q. Liu, W. Zhang, Y. Zhi, C. Wang, C. Xiao and S. Wei, *J. Am. Chem. Soc.*, 2014, **136**, 15670–15675.
- 13 Y. R. Zheng, M. R. Gao, Q. Gao, H. H. Li, J. Xu, Z. Y. Wu and S. H. Yu, *Small*, 2015, **11**, 182–188.
- 14 K. Li, J. Zhang, R. Wu, Y. Yu and B. Zhang, *Adv. Sci.*, 2016, **3**, 1500426–1500432.
- 15 D. Kong, H. Wang, Z. Lu and Y. Cui, *J. Am. Chem. Soc.*, 2014, **136**, 4897–4900.
- 16 L. F. Zhang and C. Y. Zhang, *Nanoscale*, 2014, **6**, 1782–1789.
- 17 H. T. Wang, H. W. Lee, Y. Deng, Z. Y. Lu, P. C. Hsu, Y. Y. Liu, D. C. Lin and Y. Cui, *Nat. Commun.*, 2015, **6**, 7261–7268.
- 18 S. J. Yang, T. Kim, J. H. Im, Y. S. Kim, K. Lee, H. Jung, and C. R. Park, *Chem. Mater.*, 2012, **24**, 464–470.
- 19 H. Hu, B. Guan, B. Xia and X. W. Lou, *J. Am. Chem. Soc.*, 2015, **137**, 5590–5595.
- 20 Y. Xiao, P. P. Sun and M. H. Cao, *ACS nano*, 2014, **8**, 7846–7857.
- 21 S. J. Yang, M. Antonietti and N. Fechner, *J. Am. Chem. Soc.*, 2015, **137**, 8269–8273.
- 22 A. Aijaz, N. Fujiwara and Q. Xu, *J. Am. Chem. Soc.*, 2014, **136**, 6790–6793.
- 23 X. Xu, R. Cao, S. Jeong and J. Cho, *Nano Lett.*, 2012, **12**, 4988–4991.
- 24 F. Zou, X. Hu, Z. Li, L. Qie, C. Hu, R. Zeng, Y. Jiang and Y. Huang, *Adv. Mater.*, 2014, **26**, 6622–6628.
- 25 H. Hu, L. Han, M. Yu, Z. Wang and X. W. D. Lou, *Energy Environ. Sci.*, 2016, **9**, 107–111.
- 26 J. Hao, W. Yang, Z. Zhang and J. Tang, *Nanoscale*, 2015, **7**, 11055–11062.
- 27 A. Aijaz, J. Masa, C. Rosler, W. Xia, P. Weide, A.J.R. Botz, R.A. Fischer, W. Schuhmann, M. Muhler, *Angew. Chem., Int. Edit.*, 2016, **55**, 4087–4091.
- 28 X. Y. Li, Q. Q. Jiang, S. Dou, L. B. Deng, J. Huo and S. Y. Wang, *Journal of Materials Chemistry A*, 2016, **4**, 15836–15840.
- 29 B. You, N. Jiang, M. Sheng, S. Gul, J. Yano, and Y. Sun, *Chem. Mater.*, 2015, **27**, 7636–7642. DOI: 10.1039/C5TA01453H
- 30 S. W. Li, Peng, L. S. Huang, X. Q. Cui, A. M. Al-Enizi and G. F. Zheng, *ACS Applied Materials & Interfaces*, 2016, **8**, 20534–20539.
- 31 S. Dou, L. Tao, J. Huo, S. Wang and L. Dai, *Energy Environ. Sci.*, 2016, **9**, 1320–1326.
- 32 T. Y. Ma, J. L. Cao, M. Jaroniec and S. Z. Qiao, *Angew. Chem. Int. Ed.*, 2016, **55**, 1138–1142.
- 33 G. Wu, K. L. More, C. M. Johnston, P. Zelenay, *Science*, 2011, **332**, 443–447.
- 34 Y. Zhao, K. Watanabe and K. Hashimoto, *J. Am. Chem. Soc.*, 2012, **134**, 19528–19531.
- 35 R. Ma, Y. Zhou, Y. Chen, P. Li, Q. Liu and J. Wang, *Angew. Chem. Int. Ed.*, 2015, **54**, 14723–14727.
- 36 Y. Liu, H. Jiang, Y. Zhu, X. Yang and C. Li, *J. Mater. Chem. A*, 2016, **4**, 1694–1701.
- 37 Y. Xiao and M. H. Cao, *J. Power Sources*, 2016, **305**, 1–9.
- 38 Y. Su, Y. Zhu, H. Jiang, J. Shen, X. Yang, W. Zou, J. Chen and C. Li, *Nanoscale*, 2014, **6**, 15080–15089.
- 39 K. Niu, B. Yang, J. Cui, J. Jin, X. Fu, Q. Zhao and J. Zhang, *J. Power Sources*, 2013, **243**, 65–71.
- 40 C. Zhang, R. Hao, H. Liao and Y. Hou, *Nano Energy*, 2013, **2**, 88–97.
- 41 S. G. Wang, Z. T. Cui and M. H. Cao, *Electrochim. Acta*, 2016, **210**, 328–336.
- 42 Y. Xiao, L. R. Zheng and M. H. Cao, *Nano Energy*, 2015, **12**, 152–160.
- 43 M. Shen, L. R. Zheng, W. He, C. Ruan, C. Jiang, K. Ai and L. Lu, *Nano Energy*, 2015, **17**, 120–130.
- 44 P. Chen, K. Xu, S. Tao, T. Zhou, Y. Tong, H. Ding, L. Zhang, W. Chu, C. Wu and Y. Xie, *Adv. Mater.*, 2016, **28**, 7527–7532.
- 45 H. Zhang, B. Yang, X. Wu, Z. Li, L. Lei and X. Zhang, *ACS Appl. Mater. Interfaces*, 2015, **7**, 1772–1779.
- 46 C. C. McCrory, S. Jung, J. C. Peters and T. F. Jaramillo, *J. Am. Chem. Soc.*, 2013, **135**, 16977–16987.
- 47 T. Y. Ma, S. Dai, M. Jaroniec and S. Z. Qiao, *Angew. Chem. Int. Ed.*, 2014, **53**, 7281–7285.
- 48 Y. Zhao, R. Nakamura, K. Kamiya, S. Nakanishi and K. Hashimoto, *Nat. Commun.*, 2013, **4**, 2390–2396.
- 49 X. Lv, Y. Zhu, H. Jiang, X. Yang, Y. Liu, Y. Su, J. Huang, Y. Yao and C. Li, *Dalton Transactions*, 2015, **44**, 4148–4154.
- 50 M. R. Gao, X. Cao, Q. Gao, Y. F. Xu, Y. R. Zheng, J. Jiang and S. H. Yu, *ACS Nano*, 2014, **8**, 3970–3978.
- 51 P. Ganesan, M. Prabu, J. Sanetuntikul and S. Shanmugam, *ACS Catalysis*, 2015, **5**, 3625–3637.
- 52 T. Nakagawa, N. S. Bjorge, R. W. Murray, *J. Am. Chem. Soc.*, 2009, **131**, 15578–15579.
- 53 J. Wu, Y. Xue, X. Yan, W. Yan, Q. Cheng and Y. Xie, *Nano Res.*, 2012, **5**, 521–530.
- 54 Z. Lu, H. Wang, D. Kong, K. Yan, P. C. Hsu, G. Zheng, H. Yao, Z. Liang, X. Sun and Y. Cui, *Nat. Commun.*, 2014, **5**, 4345–4352.
- 55 L. Li, S. Liu, and A. Manthiram, *Nano Energy*, 2015, **12**, 852–860.
- 56 S. G. Wang, Z. T. Cui, J. W. Qin and M. H. Cao, *Nano Res.*, 2016, **9**, 2270–2283.

The table of contents entry

In Situ Coupling of $\text{Co}_{0.85}\text{Se}$ and N-Doped Carbon via One-Step Selenizing of Metal-Organic Frameworks as Trifunctional catalysts for Overall Water Splitting and Zn-air Batteries

Tao Meng, Jinwen Qin, Shuguang Wang, Di Zhao, Baoguang Mao, Minhua Cao*



The $\text{Co}_{0.85}\text{Se}@\text{NC}$ obtained by directly selenizing ZIF-67 can be used as trifunctional catalysts for water splitting and Zn-air batteries.